Brain Struct Funct (2014) 219:1343–1353
DOI 10.1007/s00429-013-0572-0

ORIGINAL ARTICLE

An MRI atlas of the mouse basal ganglia

Jeremy F. P. Ullmann · Charles Watson · Andrew L. Janke · Nyoman D. Kurniawan · George Paxinos · David C. Reutens

Received: 22 February 2013 / Accepted: 2 May 2013 / Published online: 21 May 2013

Abstract The basal ganglia are a group of subpallial nuclei that play an important role in motor, emotional, and cognitive functions. Morphological changes and disrupted afferent/efferent connections in the basal ganglia have been associated with a variety of neurological disorders including psychiatric and movement disorders. While high-resolution magnetic resonance imaging has been used to characterize changes in brain structure in mouse models of these disorders, no systematic method for segmentation of the C57BL/6 J mouse basal ganglia exists. In this study we have used high-resolution MR images of ex vivo C57BL/6 J mouse brain to create a detailed protocol for segmenting the basal ganglia. We created a three-dimensional minimum deformation atlas, which includes the segmentation of 35 striatal, pallidal, and basal ganglia-related structures. In addition, we provide mean volumes, mean T_2 contrast intensities and mean FA and ADC values for each structure. This MR atlas is available for download, and enables researchers to perform automated segmentation in genetic models of basal ganglia disorders.

Keywords Basal ganglia · Pallidum · Striatum · Mouse brain · Atlas · Magnetic resonance imaging

Abbreviations

3D	Three-dimensional
Aca	Anterior limb of anterior commissure
AcbC	Accumbens nucleus core
AcbSh	Accumbens nucleus shell
Acp	Posterior limb of posterior commissure
ADC	Apparent diffusion coefficient
AOP	Anterior olfactory area
ASt	Amygdalostriatal transition area
B	Basal nucleus (Meynert)
cc/ec	Corpus callosum/external capsule
Ce	Central amygdaloid nucleus
CPu	Caudate putamen
DWI	Diffusion-weighted imaging
EA	Extended amygdala
EP	Entopeduncular nucleus
f	Fornix
FA	Fractional anisotropy
FOD	Fiber orientation distributions
Fu	Bed nucleus of stria terminalis, fusiform part
GP	Globus pallidus
HDB	Nucleus of the horizontal limb of the diagonal band

J. F.P. Ullmann, C. Watson and A. L. Janke contributed equally to this work.

Electronic supplementary material The online version of this article (doi:10.1007/s00429-013-0572-0) contains supplementary material, which is available to authorized users.

J. F. P. Ullmann (✉) · A. L. Janke · N. D. Kurniawan · D. C. Reutens
Center for Advanced Imaging, The University of Queensland, Brisbane, QLD 4072, Australia
e-mail: j.ullmann@uq.edu.au

C. Watson · G. Paxinos · D. C. Reutens
The Australian Mouse Brain Mapping Consortium, The University of Queensland, Brisbane, QLD, Australia

C. Watson
Health Sciences, Curtin University, Bentley, WA, Australia

G. Paxinos
Neuroscience Research Australia, The University of New South Wales, Sydney, NSW, Australia

ic	Internal capsule
ICjM	Magna island of Calleja
IEn	Intermediate nucleus of the endopiriform claustrum
IPAC	Interstitial nucleus of the post limb of the anterior commissure
LAcbSh	Accumbens nucleus shell, lateral part
LDB	Lateral nucleus of the horizontal limb of the diagonal band
LH	Lateral hypothalamus
LPO	Lateral preoptic area
LSI	Lateral septal nucleus
LSS	Lateral striatal stripe
LV	Lateral Ventricle
MDA	Minimum deformation atlas
mfb	Medial forebrain bundle
MS	Medial septal nucleus
MRI	Magnetic resonance imaging
ns	Nigrostriatal bundle
opt	Optic tract
ROI	Region of interest
SIB	Substantia innominate, part B
ST	Bed nucleus of stria terminalis
st	Stria terminalis
Tu	Olfactory tubercle
VDB	Nucleus of the vertical limb of the diagonal band
VP	Ventral pallidum

Introduction

The basal ganglia are a group of subpallial nuclei that play an important role in motor, emotional, and cognitive functions. The term 'basal ganglia' has been defined in many different ways, but we choose to restrict the meaning to include only the striatal and pallidal components of the subpallium. The striatum and pallidum have been intensively studied with modern gene expression, neurochemistry, and connectivity studies (Puelles et al. 2007; Medina and Abellan 2012). The striatum is made up of a dorsal area, the caudate and putamen, and a ventral component that consists of the accumbens nucleus, which has a core and shell subdivision (Meredith et al. 1996; Zahm and Brog 1992), the olfactory tubercle, and the Calleja islands (Heimer et al. 1982). The pallidum can also be split into its dorsal and ventral components, which include the globus pallidus and ventral pallidum, respectively. The diagonal domain, which includes the nucleus of the horizontal limb of the diagonal band, the lateral nucleus of the horizontal limb of the diagonal band, the nucleus of the vertical limb of the diagonal band, the basal nucleus (Meynert), and the substantia innominata part B is also located in the subpallial region but not considered part of the basal ganglia (*sensu strictu*). Swanson has argued that some other subpallial structures (septum, amygdala, and bed nucleus of stria terminalis) also contain elements that could be classified as striatal or pallidal (Swanson 2000), but we have not included these elements within the scope of this study.

Morphological changes and disrupted afferent and efferent connections in the basal ganglia have been associated with a variety of neurological disorders including psychiatric disorders such as schizophrenia, depression, and bipolar disorder, and movement disorders such as Parkinson's and Huntington's Disease. Animal models have become important methods for investigating the pathophysiology of these diseases and for testing potential treatments. While many species have been used to develop experimental models, including zebrafish (Panula et al. 2010; Flinn et al. 2008), rats (Pelled et al. 2007; Soria et al. 2011; Antonsen et al. 2012), and primates (Yang and Chan 2011), the mouse has become the focus of studies of development and gene expression in the basal ganglia since the advent of gene targeting in mice (Capecchi 1989).

High-field, high-resolution magnetic resonance imaging (MRI) and diffusion-weighted imaging (DWI) are increasingly being used to characterize changes in brain structure in mouse models of these disorders (Cheng et al. 2011; Cepeda-Prado et al. 2012; Lerch et al. 2008a, b; Sawiak et al. 2009a, b; Zhang et al. 2010; Boska et al. 2007; Cyr et al. 2005; Song et al. 2004; Kerbler et al. 2012). For example, volumetric measurements of structures in the mouse sub-pallium serve as measures of neurodegeneration in Huntington's disease models (Carroll et al. 2011). A definitive delineation of the anatomical structures within the mouse basal ganglia would enhance the use of MRI for phenotyping models of disease. It would establish a standard template for the anatomical localization of changes identified with voxel-based statistical parametric mapping analytical approaches. Such an anatomical template used in combination with image registration will facilitate longitudinal studies. Finally, it could be used to define regions of interest in a standardized manner.

In this study we have used high-resolution MR images of the ex vivo C57BL/6 J mouse brain to create a detailed protocol for segmenting the basal ganglia. In addition, we have created a three-dimensional atlas including average volumes, T_1/T_2^* intensities, fractional anisotropy, and apparent diffusion coefficient values.

Materials and methods

C57BL/6 J mouse brain preparation and data acquisition

Eighteen animals were perfused and fixed with 4 % paraformaldehyde and 0.1 % Magnevist® (gadopentetate dimeglumine, Bayer HealthCare Pharmaceuticals Inc., Wayne, NJ, USA) in phosphate buffer (PB). Brains were extracted and incubated in 0.1 % Magnevist/PB for 4 days, placed in Fomblin (Solvay Solexis, Milan, Italy) and imaged on a 16.4T (89 mm) Bruker micro-imaging system (Bruker Biospin, Karlsruhe, Germany) using a 15 mm SAW coil (M2 M Imaging, USA).

MRI data were acquired using a 3D gradient echo sequence with a repetition time of 50 ms, echo time of 12 ms, flip angle of 30°, 82 kHz spectral bandwidth, 8 excitations with an acquisition time of 5 h 15 min to produce T_1/T_2^*-weighted images at 30 μm^3 isotropic resolution.

HARDI data were acquired for five mice using 3D diffusion-weighted spin-echo sequence with the parameters TE/TR = 22.8/400 ms, 100 μm^3 isotropic resolution, 30 uniformly distributed DW directions, $d/D = 2.5/12.5$ ms, $b = 5{,}000$ s/mm^2, NEX = 1 with an acquisition time $\sim$32 h ($n = 5$). Fourier transformations were also performed by increasing the resolution of the k-space data by 50 % to 66 μm^3. Diffusion tensor parametric images were calculated using the program Diffusion Toolkit v0.6.2.2 (trackvis.org/dtk).

Model creation

MR images were placed in the stereotaxic Waxholm space (Johnson et al. 2010) and a symmetric model was created using a recursive non-linear hierarchical fitting strategy in a very similar fashion to Fonov et al. (2011). The final fitting step used a nonlinear transformation with a step size of 30 μm. This resulted in a model with double the resolution of the original input data (15 vs. 30 μm) (Janke et al. 2012; Ullmann et al. 2012).

Segmentation

The major anatomical features of the striatum, pallidum, associated nuclei, and fiber tracts were primarily identified on the coronal sections of the MRI model by a single expert anatomist (CW) and reviewed by another (GP). These two individuals are the authors of major rodent brain atlases (e.g. Paxinos and Franklin 2013; Paxinos et al. 2009; Watson and Paxinos 2010). The operational criteria for delineating anatomical features were defined in terms of differences in signal intensity and/or their location with reference to anatomical landmarks. The cortex was segmented into major regions and subregions using the parcellation scheme of Paxinos and Franklin (2013). In some cases our parcellation was less detailed than in the atlas, and where anatomical landmarks or clear boundaries of sub-regions could not be defined, the areas were combined. Structures were then partitioned according to the operational criteria using vector-based segmentation performed on a Cintiq tablet (Wacom Company Ltd, Vancouver, USA). The complete data set was then exported to Amira (version 5.4.4, Visualization Sciences Group, Burlington, USA) where structural boundaries were checked and corrected in the three orthogonal planes by JFPU and CW. The nomenclature and abbreviations used here were taken from Paxinos and Franklin (2013) and the color palette for cortical structures is based on that used in the BrainNavigator (Elsevier Inc., Amsterdam, Netherlands) website. Finally, smoothed three-dimensional surface reconstructions were created in Amira. Average image intensities were computed by first normalizing the intensity values in the model to lie between 0 and 100 by percent critical thresholding of the image histogram using thresholds of 0.1 and 99.9 %. The mean signal intensity for each structure was then calculated. The volume of each structure in model space was computed from the delineated labels.

Transformation of segmentation labels to DWI data and calculation of mean values

Individual fractional anisotropy (FA) and apparent diffusion coefficient (ADC) images were nonlinearly transformed to model space and the mean FA and ADC values in each structure was calculated across individuals (Collins et al. 1995).

Results

Segmentation protocol

The striatum, pallidum, and surrounding structures could be clearly visualized and sub-structures delineated in the coronal plane on the minimum deformation model. The level of contrast achieved resulted in a characteristic appearance for nearly every individual sub-structure. Segmentation is easiest to perform by partitioning the striatal and pallidal structures in relation to anatomical landmarks. The major fiber bundle landmarks (the corpus callosum (cc), the forceps minor (fmi) and the lateral external capsule (ec)) are all visible as black bands that form the dorsal border of the striatum and pallidum. In coronal sections, the anterior limb of the anterior commissure (aca) is clearly visible as a dark circular structure in the ventromedial region of each hemisphere. As one progresses caudally the

anterior part of the anterior commissure takes up a more medial position before intersecting the midline as the anterior commissure. Caudal to this, it is placed in an increasingly lateral position as the posterior part of the anterior commissure (acp). Moving caudally, as acp slowly disappears, the internal capsule (ic) becomes more prominent, with fibers projecting dorso-ventrally (Figs. 1, 2). At these levels the fornix system (f) separates into two fiber tracts that project caudoventrally, and the optic tract (opt) appears on the ventral surface of the brain before projecting dorsally along the lateral margin of the internal capsule and cerebral peduncle. Other clearly visible structures include the dark bands of the medial forebrain bundle (mfb) and olfactory tubercle (Tu) (which marks the ventral border) the bright appearance of the lateral ventricle (LV). The slightly darker stria terminalis (st) lies ventral to the lateral ventricle, and the lateral striatal stripe (LSS) which forms the medial border of the striatum and pallidum (Figs. 2, 3).

A detailed guide for segmentation for the striatal and pallidal structures is provided below, and a guide for segmentation of neighboring structures and nuclei can be found in the supplementary data section. A complete list of the segmented structures, their abbreviations, and corresponding colors is provided in Table 1, and mean volumes, signal intensities, fractional anisotropy (FA) values, and apparent diffusion coefficient (ADC) values are summarized in Table 2.

Segmentation of the striatum

Accumbens nucleus

The accumbens nucleus is a pale area between the dark patchy band of the medial forebrain bundle (mfb) below and the anterior part of the anterior commissure (aca) above. The accumbens nucleus comprises a core (AcbC) that surrounds the anterior commissure and a paler accumbens nucleus shell, which has a medial (AcbSh) and a lateral (LAcbSh) part. The accumbens shell is bounded medially by the high intensity signal of the magna island of Calleja (ICjM), laterally by the high intensity signal of the lateral striatal stripe (LSS), ventrally by the hypointense mfb, and dorsally by the dark flecks of the caudate putamen (CPu). Differentiating between the lateral and medial parts of the accumbens shell on the basis of MRI alone is very difficult but the lateral part of the accumbens shell is slightly darker than the medial part. However, the presence of reliable local landmarks makes it possible to infer the boundary on the basis of the histological subdivisions in the Paxinos and Franklin (2013) atlas. This method is less than ideal but it does provide a realistic solution where local landmarks are very strong. Lateral to the lateral striatal stripe is a region of low signal intensity, the intermediate nucleus of the endopiriform claustrum (IEn). The medial border of the accumbens nucleus is defined by the slightly lower signal

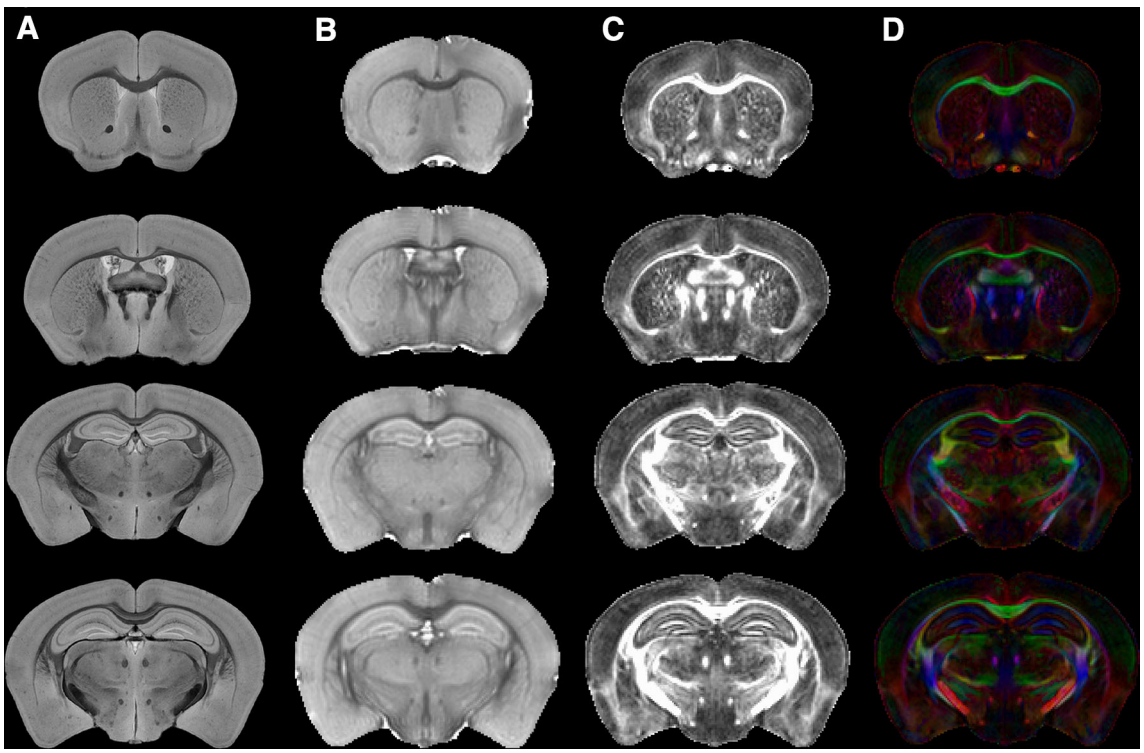

Fig. 1 Visualization of the C57BL/6 J basal ganglia on **a** 15 μm^3 MRI model, **b** apparent diffusion coefficient maps, **c** fractional anisotropy maps, and **d** color fractional anisotropy maps. (The reader is referred to the online version of this article for full color figures.)

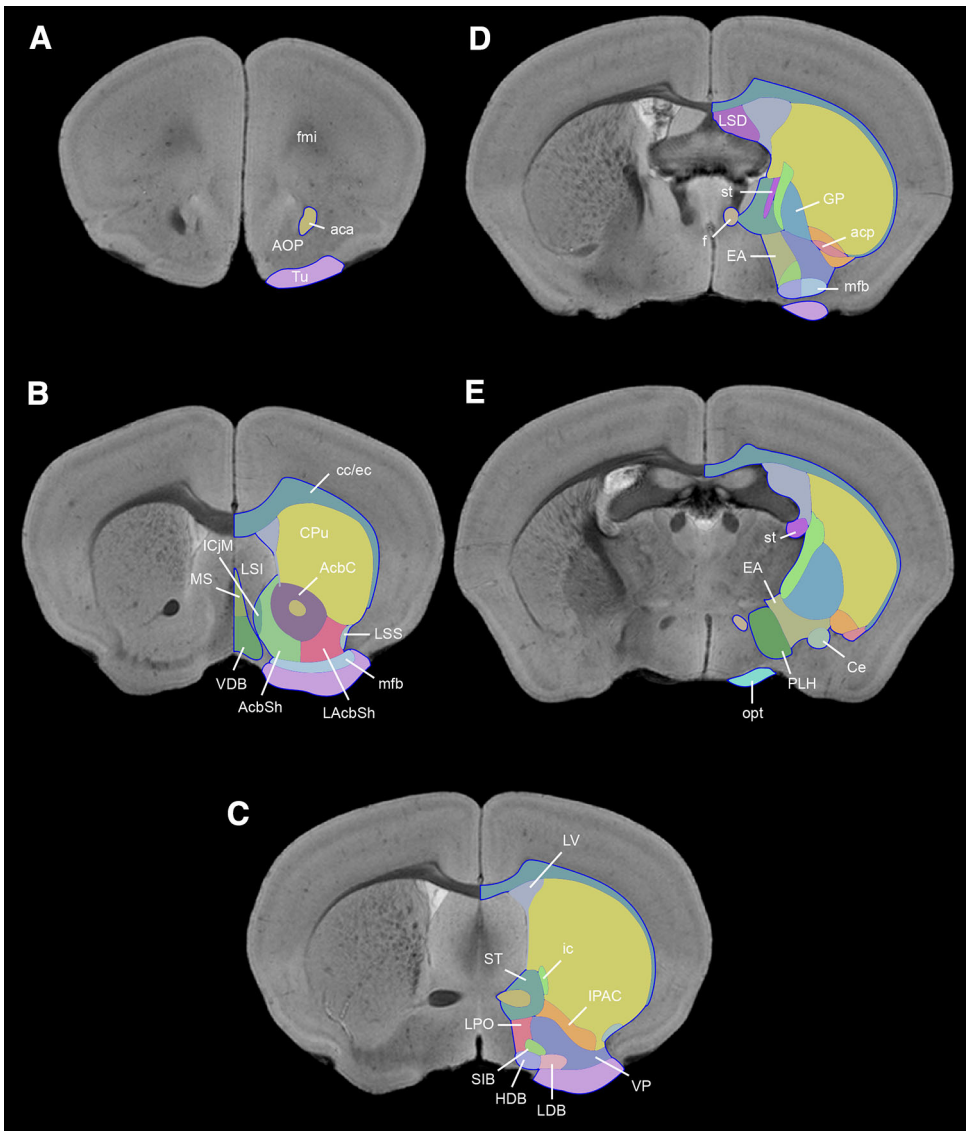

Fig. 2 Segmentation of the C57BL/6 J striatum and pallidum on representative T_1/T_2^* minimum deformation images. *aca* anterior limb of anterior commissure, *AcbC* accumbens nucleus core, *AcbSh* accumbens nucleus shell; *acp* posterior limb of posterior commissure; *AOP* anterior olfactory area; *cc/ec* corpus callosum/external capsule; *Ce* central amygdaloid nucleus; *CPu* caudate putamen; *EA* extended amygdala; *f* fornix; *fmi* forceps minor; *GP* globus pallidus; *HDB* horizontal diagonal band; *ic* internal capsule; *ICjM* Magna island of Calleja; *IPAC* interstitial nucleus of the post limb of the anterior commissure; *LAcbSh* Accumbens nucleus shell, lateral part; *LDB* lateral nucleus of the horizontal limb of the diagonal band; *LPO* lateral preoptic area; *LSD* lateral septal nucleus, dorsal part; *LSI* lateral septal nucleus, intermediate part; *LSS* lateral striatal stripe; *LV* lateral ventricle; *mfb* medial forebrain bundle; *MS* medial septal nucleus; *opt* optic tract; *PLH* peduncular part of lateral hypothalamus; *SIB* substantia innominate, basal part; *ST* bed nucleus of the stria terminalis; *st* stria terminalis; *Tu* olfactory tubercle; *VDB* nucleus of the vertical limb of the diagonal band; *VP* ventral pallidum. (The reader is referred to the online version of this article for full color figures.)

intensity of the lateral septal nucleus (LSI). At some levels, the white strip of the magna island of Calleja (ICjM) can be seen to separate the accumbens nucleus from the lateral septal nucleus. More caudally, the low signal intensity of the ventral pallidum (VP) forms the ventral and medial border of the accumbens nucleus. There is no distinct dorsal boundary between the shell of the accumbens nucleus and the caudate putamen (CPu). Consequently, our operational criterion for the border was the fiber band trailing from the anterior commissure, and the low intensity of the caudate putamen in contrast to the high intensity of the shell of the accumbens nucleus. In coronal sections at these levels, the core of the accumbens nucleus forms a very pale asymmetrical halo around the anterior commissure. At levels approaching the rostral border of the crossing of the anterior commissure, the accumbens nucleus disappears (Fig. 2c).

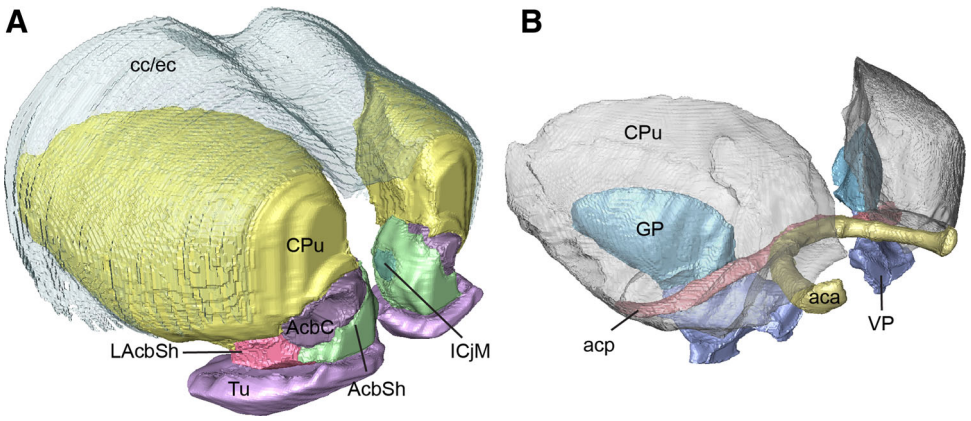

Fig. 3 Three-dimensional *polygonal* surface models of the basal ganglia. **a** Profile view of the striatum with forebrain to the *right*. *AcbC* accumbens nucleus core; *AcbSh* accumbens nucleus shell; *CPu* caudate putamen; *ICjM* Magna island of Calleja; *LAcbSh* Accumbens nucleus shell, *lateral part*; *Tu* olfactory tubercle. For anatomical reference the corpus callosum/external capsule (cc/ec) has been included transparently. **b** Profile view of the pallidum with forebrain to the *right*. *GP* globus pallidus, *VP* ventral pallidum. For anatomical reference the anterior and posterior limb of the anterior commissure, *aca* and *acp,* respectively, have been added in color and *CPu* transparently. (The reader is referred to the online version of this article for full color figures.)

Caudate putamen

The caudate putamen (CPu) is easily recognizable on account of the prominent structures that bound it. These are the corpus callosum (cc) dorsally, the external capsule (ec) laterally, and the lateral ventricle (LV), internal capsule (ic), and globus pallidus (GP) medially. The caudate putamen is continuous ventrally with the accumbens nucleus but is in general of lower signal intensity and is marked by dark flecks of projection fibers that traverse it. Medially these flecks consolidate to form the internal capsule (Fig. 2d).

Magna island of Calleja

The magna island of Calleja (ICjM) is an outstanding landmark because it forms a white strip among darker areas. It separates the shell of the accumbens nucleus from the intermediate part of the lateral septal nucleus (LSI) (Fig. 2b).

Olfactory tubercle

The olfactory tubercle (Tu) is an area of varying signal intensity between the ventral pial surface and the patchy intensity of the medial forebrain bundle dorsally. In some places, the continuity between the olfactory tubercle and the accumbens nucleus can be recognized. These pale strips are the cell bridges of the striatum. At the rostrocaudal center of the olfactory tubercle it has a distinctly layered appearance in the MR images, with a superficial dark band separated by a middle area of low signal intensity by a thin white strip that is expanded medially. The white strip represents layer 2 of the olfactory tubercle. The deeper low intensity band is in turn separated from the very dark medial forebrain bundle by an intervening light band (Fig. 2b). More rostrally, the entire olfactory tubercle is much lighter, although the bands can still be recognized. The rostral pole of the olfactory tubercle ends in the coronal plane at which the caudal end of the posterior part of the anterior olfactory area (AOP) appears (Fig. 2a).

Segmentation of the pallidum

Globus pallidus

The globus pallidus (GP) is relatively dark in comparison to the caudate putamen and interstitial nucleus of the posterior limb of the anterior commissure (IPAC), and its lateral border is easy to recognize. Medial to the globus pallidus is the black band of the internal capsule (ic). Ventrally, the rostral part of the globus pallidus is continuous with the ventral pallidum (VP) (Fig. 2d). More caudally, the ventral border of the globus pallidus is adjacent to the very pale extension of the amygdala (EA) (Fig. 2e).

Ventral pallidum

The ventral pallidum (VP) is generally of lower signal intensity than surrounding areas, and caudally it is continuous with that of globus pallidus. The most rostral part of the ventral pallidum forms a strip with patchy signal intensity between the olfactory tubercle and the accumbens nucleus. In more rostral locations, the ventral pallidum is co-extensive with the dark patches of the medial forebrain bundle. More caudally the ventral pallidum forms an

Table 1 Hierarchical segmentation of mouse basal ganglia and associated structures using the Paxinos and Franklin ontology on T_1/T_2^*-weighted images

The Mouse Brain in Stereotaxic Coordinates				The Allen Reference Atlas	
Region	**Structure Names**	**Abbreviations**	**Color Code**	**Abbreviations**	**Structure Names**
Subpallium					
Striatum					
Corpus striatum					
	Amygdalostriatal transition area	ASt			Not differentiated
	Caudate putamen	CPu		CP	Caudoputamen
	Lateral striatal stripe	LSS			Not differentiated, included into FS
Accumbens					
	Accumbens nucleus core	AcbC			
	Accumbens nucleus shell	AcbSh		ACB	Nucleus accumbens
	Accumbens nucleus shell, lateral part	LAcbSh			
	Olfactory tubercle	Tu		OT	Olfactory tubercle
Pallidum					
	Globus pallidus	GP		GPE	Globus pallidus, external segment
	Ventral pallidum	VP		SI	Substantia innominata
	Magna island of Calleja	ICjM		islm	Major island of Calleja
	Entopeduncular nucleus	EP		GPi	Globus pallidus, internal segment
Bed nucleus of the stria terminalis					
	Bed nucleus of stria terminalis	ST		BST	Bed nuclei of stria terminalis
	Bed nucleus of stria terminalis, fusiform part	Fu		BSTfu	Bed nuclei of the stria terminalis, anterior division, fusiform nucleus
Diagonal domain					
	Nucleus of the horizontal limb of the diagonal band	HDB			
	Lateral nucleus of the horizontal limb of the diagonal band	LDB		NDB	Diagonal band nucleus
	Nucleus of the vertical limb of the diagonal band	VDB			
	Basal nucleus (Meynert)	B			Not differentiated, included into SI
	Substantia innominata part B	SIB		SI	Substantia innominata
Associated structures					
	Central amygdaloid nucleus	Ce		CEA	Central amygdala nucleus
	Extension of the amygdala	EA			Not differentiated, included into LHA and SI
	Lateral hypothalamus	LH		LHA	Lateral hypothalamic area
	Interstitial nucleus of the posterior limb of the anterior commissure	IPAC		FS	Fundus of the striatum
	Lateral preoptic area	LPO		LPO	Lateral preoptic area
	Medial septal nucleus	MS		MS	Medial septal nucleus
Fiber groups					
	Anterior limb of anterior commissure	aca		aco	Anterior commissure, olfactory limb
	Posterior limb of posterior commissure	acp		act	Anterior commissure, temporal limb
	Corpus collosum/external capsule	cc/ec		cc/ec	Corpus collosum/external capsule
	Fornix	f		fx	Fornix
	Internal capsule	ic		int	Internal capsule
	Medial forebrain bundle	mfb		mfb	Medial forebrain bundle
	Nigrostriatal bundle	ns		ntt	Nigrostriatal tract
	Optic tract	opt		opt	Optic tract
	Stria terminalis	st		st	Stria terminalis
Ventricles					
	Lateral Ventricle	LV		VL	Lateral ventricle

For each structure the name and abbreviation is provided according to Paxinos and Franklin and the Allen Reference Atlas and a color code for the region is given

extensive low intensity region stretching from the olfactory tubercle to the anterior commissure, where it contacts parts of the bed nucleus of the stria terminalis (diagonal domain) (ST). The medial border of the ventral pallidum is formed by the basal part of the substantia innominate part B (SIB) and the lateral preoptic area (LPO). The dorsolateral border is formed by the interstitial nucleus of the post limb of the anterior commissure (IPAC), which is very pale, almost white, in these images (Fig. 2c). More caudally, the ventral pallidum is bounded ventrally by the distinct low intensity of the lateral nucleus of the diagonal band (LDB). The lateral nucleus of the diagonal band (formerly called the magnocellular preoptic nucleus) occupies the same territory as the medial forebrain bundle and is consequently a very dark area. Immediately caudal to the crossing of the anterior commissure, the ventral pallidum is continuous dorsally with the globus pallidus and is in contact with the bed nucleus of the stria terminalis. At these caudal levels, the ventral pallidum is bordered medially by the extension of the amygdala, which is a wide pale band stretching from

the lateral diagonal band ventrally to the bed nucleus of the stria terminalis dorsally (Fig. 2d). The most caudal part of the ventral pallidum is bounded ventrally by the anterior amygdaloid area, which is similar in intensity to the ventral pallidum, and therefore a distinct border cannot be ascertained. We suggest using the section that contains the hippocampal commissure as a rough demarcation of the transition of the ventral pallidum to the anterior amygdaloid area.

Discussion

Imaging considerations

This study presents an MRI-based C57BL/6 J atlas of the mouse basal ganglia. We describe a protocol for segmenting 35 striatal, pallidal, and basal ganglia-related structures. While numerous MRI-based atlases of the basal ganglia exist for human and non-human primates (Sadikot et al. 2011; Ahsan et al. 2007; Yelnik et al. 2007; Deogaonkar et al. 2005; Francois et al. 1996; Lanciego and Vazquez 2012; Saleem and Logothetis 2007), this is the first MRI-based atlas of the rodent basal ganglia. Similar to previous studies our segmentation protocol and atlas were created based upon on a minimum deformation atlas, which represents the average intensity, and therefore average anatomy, of 18 brains (MacKenzie-Graham et al. 2007; Janke et al. 2012; Ullmann et al. 2012). This approach accounts for individual anatomical variability or variance introduced in the preparation of individual brains. Consequently, the minimum deformation atlas provides better contrast and enhances structural delineations. This is best exemplified by the ability to visualize and segment fine structures such as the Magna island of Calleja (Fig. 2).

To facilitate segmentation we also collected a small number of diffusion-weighted imaging (DWI) data sets. Over the past decade the use DWI has grown significantly as it provides novel contrasts that reflect tissue diffusivity. DWI has been applied to the mouse brain and numerous developmental and adult atlases have been created (Jiang and Johnson 2011; Chuang et al. 2011; Zhang et al. 2003). Studies in the rat have also demonstrated the utility of DWI for segmentation of brain regions (Johnson et al. 2012). As a result, we collected DWI data sets with the expectation that the data would assist in structural identification within the mouse basal ganglia. However, the spatial resolution in our acquired DWI images was significantly less than our T_1/T_2^* spatial resolution (100 vs. 30 μm^3) and therefore did not facilitate delineations of the basal ganglia or associated structures. While other studies have achieved a higher resolution, such as 43 μm^3 by Jiang and Johnson (2011), they collected a fewer number of diffusion directions than we did (6 vs. 30, respectively). We opted to acquire data sets with a larger number of diffusion directions but a lower resolution because it allowed us to calculate more accurate fiber orientation distributions (FOD) (Tournier et al. 2007, 2012). However, the improved FODs did not compensate for partial volume effects and as a result we did not find the DWI data sets to be useful for segmentations.

A possible way to improve upon our existing DWI data would be to register the data sets into a single atlas using a comparable methodology utilized to create our T_1/T_2^* model. As in the T_1/T_2^* MDA registration, this should produce a DWI atlas with reduced noise in the diffusion index estimations and fewer random errors, resulting in more accurate ADC and FA maps (Jiang and Johnson 2011). It is interesting to note that our FA values were lower from those obtained by Jiang and Johnson (2011). This is most likely due to using a higher *b*-value and using regions of interest (ROI's) defined on structural imaging. Structural imaging ROIs are generally larger than those defined via tract based measures due to partial volume effects. Our average ROI FA values reflect the entire structure (glial tissue, etc.) and not just the average FA of the tracts in the ROI's.

Another method which could be used to assist in segmentation of T_1/T_2^* images is registering histological data back to the individual or model. Following imaging, the brain is processed histologically and every section is collected. Subsequently, the sections are digitally stacked into a reconstructed volume and non-linearly transformed back to the MRI of an individual brain or a model (Chakravarty et al. 2008; Choe et al. 2011; Yang et al. 2012). To date this technique has primarily been used to reconstruct Nissl stained sections (Yang et al. 2012; Johnson et al. 2010), however, it is feasible that brains labeled with other markers could also be used. This would allow genetic makers to be employed to delineate divisions of the brain on the MRI data. For example, markers for cadherin could be used to segment the basal ganglia (Hertel et al. 2008). However, published protocols for utilizing the same samples for MRI and immunohistochemistry or in situ hybridizations are not yet available.

Ontological considerations

In this paper, we have restricted our definition of the basal ganglia to include only the striatum and pallidum on the basis that both structures are subpallial and both are related to motor functions (Brodal 2004; Watson et al. 2010). However, significant controversy exists regarding the structures included in the term 'basal ganglia'. For example, in the past the amygdala has been included with the

Table 2 For each structure that neighbors the striatum or pallidum, we have calculated mean values for a number of parameters including volume, signal intensity as a percent of the maximum, apparent diffusion coefficient (ADC) value, and fractional anisotropy (FA) value

Structure	Mean volume (mm^3)	Mean signal intensity (%)	ADC (Mean ± SD)	FA (Mean ± SD)
aca	0.446	46.314	7.51E−05 ± 1.28E−05	5.22E−02 ± 3.72E−03
AcbC	1.447	70.611	2.55E−04 ± 3.62E−05	1.73E−01 ± 3.70E−02
AcbSh	1.352	70.318	2.54E−04 ± 4.72E−05	1.79E−01 ± 2.63E−02
acp	0.242	55.943	2.00E−04 ± 4.94E−05	1.06E−01 ± 3.08E−02
ASt	0.305	72.890	2.72E−04 ± 2.88E−05	1.91E−01 ± 3.40E−02
B	0.007	60.882	2.97E−04 ± 2.85E−05	2.13E−01 ± 3.43E−02
cc/ec	5.355	50.586	2.68E−04 ± 4.70E−05	2.13E−01 ± 7.35E−02
Ce	0.817	71.162	2.60E−04 ± 3.32E−05	2.19E−01 ± 2.87E−02
CPu	20.298	65.757	2.71E−04 ± 4.31E−05	2.02E−01 ± 3.27E−02
EA	0.644	63.810	2.72E−04 ± 3.39E−05	1.91E−01 ± 2.72E−02
EP	0.236	50.283	2.45E−04 ± 2.76E−05	2.08E−01 ± 5.03E−02
f	0.259	52.044	2.12E−04 ± 2.86E−05	2.11E−01 ± 1.19E−02
Fu	0.003	68.511	2.22E−04 ± 2.11E−05	1.98E−01 ± 2.00E−02
GP	2.109	56.874	2.48E−04 ± 4.30E−05	1.58E−01 ± 2.46E−02
HDB	0.373	60.942	2.65E−04 ± 3.87E−05	1.67E−01 ± 5.97E−02
ic	2.024	44.186	2.53E−04 ± 7.02E−05	1.53E−01 ± 4.19E−02
ICjM	0.059	73.733	2.47E−04 ± 3.09E−05	1.90E−01 ± 2.68E−02
IPAC	0.721	69.388	2.41E−04 ± 6.15E−05	1.33E−01 ± 3.11E−02
LAcbSh	0.569	68.604	2.82E−04 ± 4.12E−05	1.87E−01 ± 2.57E−02
LDB	0.144	60.158	1.56E−04 ± 5.21E−05	9.71E−02 ± 1.38E−02
LH	0.485	60.223	2.74E−04 ± 9.44E−05	1.65E−01 ± 2.76E−02
LPO	0.063	64.577	2.25E−04 ± 2.06E−05	1.69E−01 ± 2.14E−02
LSS	0.101	68.147	2.52E−04 ± 5.35E−05	1.52E−01 ± 1.63E−02
LV	2.378	73.501	1.61E−04 ± 6.09E−05	1.37E−01 ± 1.74E−02
mfb	0.946	61.426	2.43E−04 ± 2.13E−05	2.25E−01 ± 2.97E−02
MS	0.149	58.170	8.80E−05 ± 2.33E−05	5.73E−02 ± 7.50E−03
ns	0.179	65.387	2.24E−04 ± 3.71E−05	1.48E−01 ± 2.11E−02
opt	0.825	36.594	2.18E−04 ± 1.66E−05	2.31E−01 ± 3.89E−02
SIB	0.137	63.436	2.24E−04 ± 1.94E−05	2.23E−01 ± 2.39E−02
ST	0.436	58.942	2.74E−04 ± 5.88E−05	1.89E−01 ± 3.47E−02
st	0.784	73.439	2.42E−04 ± 3.66E−05	2.35E−01 ± 5.45E−02
Tu	2.737	65.013	2.44E−04 ± 3.45E−05	2.12E−01 ± 2.91E−02
VDB	0.33	63.116	1.38E−05 ± 1.08E−05	8.43E−03 ± 4.69E−03
VP	1.087	62.767	2.39E−04 ± 7.56E−05	1.22E−01 ± 3.30E−02

striatum and pallidum, because of shared subpallial origins, even though the amygdala is anatomically and functionally very different (Swanson and Petrovich 1998). For example, some nuclei of the amygdala use glutamate as neurotransmitter, whereas projections from the striatum utilize GABA (Swanson and Petrovich 1998). The amygdala also differs from the basal ganglia as it is a key center of the gustatory-viscerocceptive and nociceptive systems and plays an important role in generating emotional responses such as anxiety, fear, and reward states (Medina and Abellan 2012; Martinez-Garcia et al. 2012).

Definitions of the basal ganglia in major textbooks have sometimes included the subthalamic nucleus and substantia nigra, on the basis of related motor functions (e.g. Bear et al. 2007; Gerfen 2004; Oorschot 2010). The objection to this approach is that neither of these two structures belongs to the subpallium; they belong instead to quite different regions of the brain. Modern gene expression studies have shown that the subthalamic nucleus in part of the hypothalamus (Puelles et al. 2012) and the substantia nigra stretches from the rostral hindbrain, across the midbrain, to the diencephalon (Puelles et al. 2007, 2012).

Conclusion

This study presents an atlas of the C57BL/6 J mouse basal ganglia and associated structures. The work presented here complements previously established MRI-based atlases of the mouse brain by providing a higher resolution model and a segmentation of the basal ganglia. To facilitate its use we have placed the atlas into standard mouse brain reference spaces, including the digital Waxholm Space (Johnson et al. 2010) and the histological Paxinos and Franklin mouse brain space (Paxinos and Franklin 2013). The segmentation method and atlas we have established is available for future studies that would like to analyze the basal ganglia and can be downloaded at http://www.imaging.org.au/AMBMC/Basal_ganglia.

Acknowledgments This work was supported by the National Health and Medical Research Council (NHMRC) of Australia (grant number 436673) and a National Computational Infrastructure Grant (grant dc0). Paxinos and Watson were supported by an Australia fellowship to GP. We would like to thank National Imaging Facility (NIF) and Queensland NMR Network (QNN) for access to the 16.4T scanner and technical support. In addition, we would like to thank Dr. Marianne Keller and the other members of AMBMC.

References

Ahsan RL, Allom R, Gousias IS, Habib H, Turkheimer FE, Free S, Lemieux L, Myers R, Duncan JS, Brooks DJ, Koepp MJ, Hammers A (2007) Volumes, spatial extents and a probabilistic atlas of the human basal ganglia and thalamus. NeuroImage 38(2):261–270

Antonsen BT, Jiang Y, Veraart J, Qu H, Nguyen HP, Sijbers J, von Horsten S, Johnson GA, Leergaard TB (2013) Altered diffusion tensor imaging measurements in aged transgenic Huntington disease rats. Brain Struct Funct 218:767–778

Bear M, Conners B, Paradiso M (2007) Neuroscience. Exploring the brain, 3rd edn. Lippincott Williams & Wilkins, Baltimore

Boska MD, Hasan KM, Kibuule D, Banerjee R, McIntyre E, Nelson JA, Hahn T, Gendelman HE, Mosley RL (2007) Quantitative diffusion tensor imaging detects dopaminergic neuronal degeneration in a murine model of Parkinson's disease. Neurobiol Dis 26(3):590–596

Brodal P (2004) The central nervous system, 4th edn. Oxford University Press, New York

Capecchi MR (1989) The new mouse genetics: altering the genome by gene targeting. Trends Genet 5(3):70–76

Carroll JB, Lerch JP, Franciosi S, Spreeuw A, Bissada N, Henkelman RM, Hayden MR (2011) Natural history of disease in the YAC128 mouse reveals a discrete signature of pathology in Huntington disease. Neurobiol Dis 43(1):257–265

Cepeda-Prado E, Popp S, Khan U, Stefanov D, Rodriguez J, Menalled LB, Dow-Edwards D, Small SA, Moreno H (2012) R6/2 Huntington's disease mice develop early and progressive abnormal brain metabolism and seizures. J Neurosci 32(19): 6456–6467

Chakravarty MM, Bedell BJ, Zehntner SP, Evans AC, Collins DL (2008) Three-dimensional reconstruction of serial histological mouse brain sections. In: 2008 IEEE international symposium on biomedical imaging: from nano to macro, vol 1–4, pp 987–990

Cheng Y, Peng Q, Hou Z, Aggarwal M, Zhang J, Mori S, Ross CA, Duan W (2011) Structural MRI detects progressive regional brain atrophy and neuroprotective effects in N171–82Q Huntington's disease mouse model. Neuroimage 56(3):1027–1034

Choe AS, Gao YR, Li X, Compton KB, Stepniewska I, Anderson AW (2011) Accuracy of image registration between MRI and light microscopy in the ex vivo brain. Magn Reson Imaging 29(5):683–692

Chuang N, Mori S, Yamamoto A, Jiang H, Ye X, Xu X, Richards LJ, Nathans J, Miller MI, Toga AW, Sidman RL, Zhang J (2011) An MRI-based atlas and database of the developing mouse brain. NeuroImage 54(1):80–89

Collins DL, Holmes CJ, Peters TM, Evans AC (1995) Automatic 3-D model-based neuroanatomical segmentation. Hum Brain Mapp 3(3):190–208

Cyr M, Caron MG, Johnson GA, Laakso A (2005) Magnetic resonance imaging at microscopic resolution reveals subtle morphological changes in a mouse model of dopaminergic hyperfunction. NeuroImage 26(1):83–90

Deogaonkar M, Heers M, Mahajan S, Brummer M, Subramanian T (2005) Method of construction of a MRI-based tabular database of 3D stereotaxic co-ordinates for individual structures in the basal ganglia of *Macaca mulatta*. J Neurosci Meth 149(2): 154–163

Flinn L, Bretaud S, Lo C, Ingham PW, Bandmann O (2008) Zebrafish as a new animal model for movement disorders. J Neurochem 106(5):1991–1997

Fonov V, Evans AC, Botteron K, Almli CR, McKinstry RC, Collins DL (2011) Unbiased average age-appropriate atlases for pediatric studies. NeuroImage 54(1):313–327

Francois C, Yelnik J, Percheron G (1996) A stereotaxic atlas of the basal ganglia in macaques. Brain Res Bull 41(3):151–158

Gerfen CR (2004) Basal Ganglia. In: Paxinos G (ed) The rat nervous system, 3rd edn. Elsevier Academic Press, San Diego, pp 455–508

Heimer L, Switzer RD, Van Hoesen GW (1982) Ventral striatum and ventral pallidum components of the motor system? Trends Neurosci 5(3):83–87

Hertel N, Krishna K, Nuernberger M, Redies C (2008) A cadherin-based code for the divisions of the mouse basal ganglia. J Comp Neurol 508(4):511–528

Janke AL, Ullmann JFP, Kurniawan ND, Paxinos G, Keller M, Yang Z, Richards K, Egan G, Petrou S, Galloway G, Reutens D (2012) 15 μm average mouse models in Waxholm space from 16.4T 30 μm images. In: 20th annual ISMRM scientific meeting and exhibition, Melbourne, Australia

Jiang Y, Johnson GA (2011) Microscopic diffusion tensor atlas of the mouse brain. NeuroImage 56(3):1235–1243

Johnson GA, Badea A, Brandenburg J, Cofer G, Fubara B, Liu S, Nissanov J (2010) Waxholm space: an image-based reference for coordinating mouse brain research. NeuroImage 53(2):365–372

Johnson GA, Calabrese E, Badea A, Paxinos G, Watson C (2012) A multidimensional magnetic resonance histology atlas of the Wistar rat brain. NeuroImage 62(3):1848–1856

Kerbler GM, Hamlin AS, Pannek K, Kurniawan ND, Keller MD, Rose SE, Coulson EJ (2012) Diffusion-weighted magnetic resonance imaging detection of basal forebrain cholinergic degeneration in a mouse model. NeuroImage 66C:133–141

Lanciego JL, Vazquez A (2012) The basal ganglia and thalamus of the long-tailed macaque in stereotaxic coordinates. A template atlas based on coronal, sagittal and horizontal brain sections. Brain Struct Funct 217(2):613–666

Lerch JP, Carroll JB, Dorr A, Spring S, Evans AC, Hayden MR, Sled JG, Henkelman RM (2008a) Cortical thickness measured from MRI in the YAC128 mouse model of Huntington's disease. NeuroImage 41(2):243–251

Lerch JP, Carroll JB, Spring S, Bertram LN, Schwab C, Hayden MR, Henkelman RM (2008b) Automated deformation analysis in the YAC128 Huntington disease mouse model. NeuroImage 39(1):32–39

MacKenzie-Graham A, Boline J, Toga AW (2007) Brain atlases and neuroanatomic imaging. Methods Mol Biol 401:183–194

Martinez-Garcia G, Novejarque A, Gutierrez-Castellanos N, Lanuza E (2012) Piriform cortex and amygdala. In: Watson C, Paxinos G, Puelles L (eds) The mouse nervous system, vol 1. Elsevier Academic Press, San Diego, pp 140–172

Medina L, Abellan A (2012) Subpallial structures. In: Watson C, Paxinos G, Puelles L (eds) The mouse nervous system, vol 1. Elsevier Academic Press, San Diego, pp 173–220

Meredith GE, Pattiselanno A, Groenewegen HJ, Haber SN (1996) Shell and core in monkey and human nucleus accumbens identified with antibodies to calbindin-D28 k. J Comp Neurol 365(4):628–639

Oorschot DE (2010) Cell types in the different nuclei of the basal ganglia. In: Steiner H, Tseng KY (eds) Handbook of basal ganglia structure and function. Elsevier Inc., San Diego, pp 63–74

Panula P, Chen YC, Priyadarshini M, Kudo H, Semenova S, Sundvik M, Sallinen V (2010) The comparative neuroanatomy and neurochemistry of zebrafish CNS systems of relevance to human neuropsychiatric diseases. Neurobiol Dis 40(1):46–57

Paxinos G, Franklin K (2013) The mouse brain in stereotaxic coordinates, vol 4. Academic Press, San Diego

Paxinos G, Watson C, Carrive P, Kirkcaldie MT, Ashwell K (2009) Chemoarchitectonic atlas of the rat brain. Elsevier Academic Press, San Diego

Pelled G, Bergman H, Ben-Hur T, Goelman G (2007) Manganese-enhanced MRI in a rat model of Parkinson's disease. J Magn Reson Imaging 26(4):863–870

Puelles L, Martinez-de-la-Torre M, Paxinos G, Watson C, Martinez S (2007) The chick brain in stereotaxic coordinates. An atlas featuring neuromeres and mammalian homologies. Elsevier Academic Press, San Diego

Puelles E, Martinez-de-la-Torre M, Watson C, Puelles L (2012) Midbrain. In: Watson C, Paxinos G, Puelles L (eds) The mouse nervous system, vol 1. Elsevier Academic Press, San Diego, pp 337–359

Sadikot AF, Chakravarty MM, Bertrand G, Rymar VV, Al-Subaie F, Collins DL (2011) Creation of computerized 3D MRI-integrated atlases of the human basal ganglia and thalamus. Front Syst Neurosci 5:71

Saleem K, Logothetis N (2007) A combined MRI and histology atlas of the rhesus monkey brain in stereotaxic coordinates. Academic Press, San Diego

Sawiak SJ, Wood NI, Williams GB, Morton AJ, Carpenter TA (2009a) Use of magnetic resonance imaging for anatomical phenotyping of the R6/2 mouse model of Huntington's disease. Neurobiol Dis 33(1):12–19

Sawiak SJ, Wood NI, Williams GB, Morton AJ, Carpenter TA (2009b) Voxel-based morphometry in the R6/2 transgenic mouse reveals differences between genotypes not seen with manual 2D morphometry. Neurobiol Dis 33(1):20–27

Song SK, Kim JH, Lin SJ, Brendza RP, Holtzman DM (2004) Diffusion tensor imaging detects age-dependent white matter changes in a transgenic mouse model with amyloid deposition. Neurobiol Dis 15(3):640–647

Soria G, Aguilar E, Tudela R, Mullol J, Planas AM, Marin C (2011) In vivo magnetic resonance imaging characterization of bilateral structural changes in experimental Parkinson's disease: a T2 relaxometry study combined with longitudinal diffusion tensor imaging and manganese-enhanced magnetic resonance imaging in the 6-hydroxydopamine rat model. Eur J Neurosci 33(8): 1551–1560

Swanson LW (2000) Cerebral hemisphere regulation of motivated behavior. Brain Res 886(1–2):113–164

Swanson LW, Petrovich GD (1998) What is the amygdala? Trends Neurosci 21(8):323–331

Tournier JD, Calamante F, Connelly A (2007) Robust determination of the fibre orientation distribution in diffusion MRI: non-negativity constrained super-resolved spherical deconvolution. NeuroImage 35(4):1459–1472

Tournier JD, Calamante F, Connelly A (2012) MRtrix: diffusion tractography in crossing fiber regions. Int J Imaging Syst Tech 22(1):53–66

Ullmann JF, Keller MD, Watson C, Janke AL, Kurniawan ND, Yang Z, Richards K, Paxinos G, Egan GF, Petrou S, Bartlett P, Galloway GJ, Reutens DC (2012) Segmentation of the C57BL/6 J mouse cerebellum in magnetic resonance images. NeuroImage 62(3):1408–1414

Watson C, Paxinos G (2010) Chemoarchitectonic atlas of the mouse brain. Elsevier Academic Press, San Diego

Watson C, Kirkcaldie MT, Paxinos G (2010) The brain: an introduction to functional neuroanatomy. Academic Press, San Diego

Yang SH, Chan AW (2011) Transgenic animal models of Huntington's disease. Curr Top Behav Neurosci 7:61–85

Yang Z, Richards K, Kurniawan ND, Petrou S, Reutens DC (2012) MRI-guided volume reconstruction of mouse brain from histological sections. J Neurosci Meth 211(2):210–217

Yelnik J, Bardinet E, Dormont D, Malandain G, Ourselin S, Tande D, Karachi C, Ayache N, Cornu P, Agid Y (2007) A three-dimensional, histological and deformable atlas of the human basal ganglia. I. Atlas construction based on immunohistochemical and MRI data. NeuroImage 34(2):618–638

Zahm DS, Brog JS (1992) On the significance of subterritories in the "accumbens" part of the rat ventral striatum. Neuroscience 50(4):751–767

Zhang J, Richards LJ, Yarowsky P, Huang H, van Zijl PCM, Mori S (2003) Three-dimensional anatomical characterization of the developing mouse brain by diffusion tensor microimaging. NeuroImage 20(3):1639–1648

Zhang JY, Peng Q, Li Q, Jahanshad N, Hou ZP, Jiang ML, Masuda N, Langbehn DR, Miller MI, Mori S, Ross CA, Duan WZ (2010) Longitudinal characterization of brain atrophy of a Huntington's disease mouse model by automated morphological analyses of magnetic resonance images. Neuroimage 49(3):2340–2351